American Mineralogist, Volume 104, pages 671–678, 2019

Melting curve minimum of barium carbonate $BaCO_3$ near 5 GPa

JUNJIE DONG[1,*,§], JIE LI[1,†], FENG ZHU[1,‡], ZEYU LI[1], AND RAMI FARAWI[1]

[1]Department of Earth and Environmental Sciences, University of Michigan, Ann Arbor, Michigan 48109, U.S.A.

ABSTRACT

The melting point of barium carbonate ($BaCO_3$) was determined at pressures up to 11 GPa using the ionic conductivity and platinum (Pt) sphere methods in a multi-anvil press. The melting point decreases with pressure from 2149 ± 50 K at 3 GPa to a fitted local minimum of 1849 K at 5.5 GPa, and then it rises with pressure to 2453 ± 50 K at 11 GPa. The fitted melting curve of $BaCO_3$ based on the ionic conductivity measurements is consistent with the Pt sphere measurements that were carried out independently at selected pressures. The negative slope of the $BaCO_3$ melting curve between 3 and 5.5 GPa indicates that the liquid is denser than the solid within this pressure range. Synchrotron X-ray diffraction (XRD) measurements in a laser-heated diamond-anvil cell (LH-DAC) showed that $BaCO_3$ transformed from the aragonite structure (*Pmcn*) to the post-aragonite structure (*Pmmn*) at 6.3 GPa and 1026 K as well as 8 GPa and 1100 K and the post-aragonite structure remained metastable upon quenching and only reverted back to the witherite structure upon pressure release. The local minimum near 5 GPa is attributed to the triple point where the melting curve of $BaCO_3$ meets a phase transition to the denser post-aragonite structure (*Pmmn*). Local minima in the melting curves of alkaline earth carbonates would lead to incipient melting of carbonated rocks in Earth's mantle.

Keywords: Barium carbonate, melting point, density crossover, phase transition, negative melting slope, post-aragonite structure; Earth in Five Reactions: A Deep Carbon Perspective

INTRODUCTION

Alkaline earth carbonates, primarily $CaCO_3$ and $MgCO_3$, play important roles in transporting carbon into the deep mantle through subducting slabs (e.g., Dasgupta 2013). A recent study suggests a local minimum in the melting curve of $CaCO_3$ near 13 GPa, likely resulting from a phase transition that intersects the melting curve, but the inferred negative melting slope is not clearly resolved (Li et al. 2017). Another alkaline earth carbonate, $BaCO_3$, is shown to undergo similar pressure-induced aragonite to post-aragonite phase transition as $CaCO_3$ but at lower pressures (Shatskiy et al. 2015). Investigating the melting behavior of $BaCO_3$ will allow for testing the occurrence of solid-liquid density crossover in compressed alkaline earth carbonates. Furthermore, systematic comparison of the structure and stability of alkaline earth carbonates is useful for constructing thermodynamic models to predict the melting behavior of complex mantle rocks in a petrologically relevant pressure-temperature-composition space (Hurt and Wolf 2018).

The melting behavior of $BaCO_3$ at 1 bar is currently unresolved. The reported melting point ranges from 1084 K in the Material Safety Data Sheets (MSDS) provided by Alfa Aesar (ThermoFisher Scientific 2010), 1653 K in the National Standard Reference Data System (Stern and Weise 1969) to 1828 K in the CRC Handbook of Chemistry and Physics (Rumble 2018). Some studies suggest that $BaCO_3$ decomposes in the solid state to BaO and CO_2 (Arvanitidis et al. 1996). Data on the melting behavior of $BaCO_3$ at higher pressures are not available. In this study, the melting curve of $BaCO_3$, as well as the phase boundary between the aragonite and post-aragonite phases of $BaCO_3$, were investigated experimentally at upper mantle conditions. The results were applied to examine the influence of solid-solid transitions on the shape of the melting curve and explore the implications for the melting behavior of carbonated rocks in Earth's mantle.

METHODS

Fine powder of high-purity $BaCO_3$ (Alfa Aesar 10645, 99.997%) was used as the starting material. Prior to experiments, the sample was kept in a vacuum oven at 400 K to remove moisture.

Multi-anvil experiments

Ionic conductivity experiments were performed at pressures between 3 and 11 GPa using a 1000-ton Walker-type multi-anvil press at the University of Michigan. Toshiba-Tungaloy F-grade tungsten carbide cubes with 5 mm truncation edge length (TEL) and the COMPRESS 10/5 assembly (Leinenweber et al. 2012) were used to generate high pressures and high temperatures. Closed high-pressure cell assemblies were dried in a vacuum oven at 400 K for 8–24 h before loading into the multi-anvil press. The uncertainty in pressure measurement is estimated to be ±7%. This includes the precision of pressure calibration of ±5% estimated on the basis of duplicate experiments, and systematic errors of ±5% arising from the effect of temperature on pressure calibration and pressure drift during heating and cooling (Li and Li 2015). A standard type-C thermocouple (TC) was used to monitor temperature. The uncertainty in the measured temperature is estimated to be ±50 K. This includes the precision in the thermocouple calibration and the position of the TC junction relative to the sample (Li and Li 2015) but ignores the effect of pressure on the electromotive force (emf) of the TC. Limited data suggest that the type-C TC underestimates temperature and that systematic error generally increases with pressure and temperature, rising to tens of degrees at 10 GPa and above 2000 K (Li et al. 2003). As a result, the measured melting points of $BaCO_3$ at >10 GPa may be

---

[*] E-mail: junjiedong@g.harvard.edu. Present address: Department of Earth and Planetary Sciences, Harvard University, Cambridge, Massachusetts 02138, U.S.A. Orcid 0000-0003-1114-9348.

[†] Orcid 0000-0003-4761-722X.

[‡] Present address: Hawaii Institute of Geophysics and Planetology, University of Hawai'i at Mānoa, Honolulu, Hawaii, U.S.A. Orcid 0000-0003-2409-151X.

[§] Special collection papers can be found online at http://www.minsocam.org/MSA/AmMin/special-collections.html.

0003-004X/19/0005–671$05.00/DOI: https://doi.org/10.2138/am-2019-6891

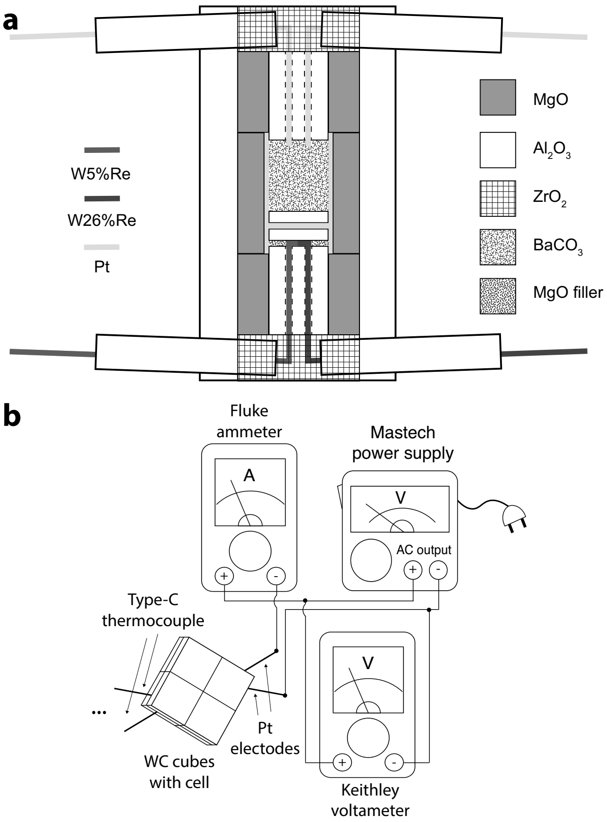

FIGURE 1. Experimental configuration of ionic conductivity measurements in a multi-anvil press. (**a**) Configuration of the modified COMPRES 5 mm cell assembly. The electrodes and the thermocouple were placed symmetrically along the rotational axis of the cell assembly for reliable measurements of melting temperature. (**b**) Pictorial diagram of the circuit with a type-C thermocouple and a pair of Pt electrodes.

lower than the real values by a few tens of degrees.

The cell assembly for the ionic conductivity measurements (Fig. 1a) was modified from the COMPRESS 10/5 assembly, similar to that of Li et al. (2017). Two pairs of slots were cut at both ends of the Re furnace and the $LaCrO_3$ sleeve to fit the TC and Pt electrode wires. A pair of Pt wires were inserted into one of the four-bore Al_2O_3 tubing and served as the electrodes. Each 4-bore alumina (Al_2O_3) tubing was enclosed in a Pt tubing, which was further surrounded by a magnesia (MgO) sleeve. The electrode tips and TC junction were placed along the rotational axis of the cylindrical-shaped heater and at the same distance to the equator of the heater so that the TC measured the temperature at the electrode tips. Both the TC junction and electrode tips were positioned within the middle third of the heater length, where the temperature gradient is estimated to be less than 100 K (Leinenweber et al. 2012).

The circuit for ionic conductivity measurements (Fig. 1b) includes a Mastech variable transformer and a Fluke 289 multi-meter. External electromagnetic interference, including heating current and the pressure control motor, is less than a few microamps and negligible compared with the ionic current through molten $BaCO_3$.

In a typical experiment, the ionic current through the compressed sample was monitored during multiple heating and cooling cycles at a given pressure, and the same recording procedure was repeated at several pressures along its compressional path. The sample was pressurized at a rate of 1 to 3 GPa per hour to the target pressure and then heated at a rate of 60 K per minute. In some experiments, the assembly was sintered at 1273 K for 1–2 h, and then further heated until a current jump was detected. After heating, the sample was cooled at the rate of 180 K per minute to 1473 K and then heated up again for more heating cycles to repeat the melting detection. At each pressure, at least two heating cycles were completed before the sample was compressed to the next target pressure. Melting measurements were repeated multiple times at different pressures in each experiment. At the highest pressure and temperature of each experiment, the sample was quenched by turning off the power.

To cross-validate the ionic conductivity measurements, Pt sphere experiments without electrodes were conducted independently using the same multi-anvil press. During sample loading, a Pt sphere of 100 to 200 μm in diameter was placed near the top of the sample. After heating and recovering the sample, the location of the Pt sphere was used to determine whether the sample was molten or not at the target temperature. Pt sphere experiments at 5.5 and 8 GPa used the standard COMPRESS 10/5 assembly with Pt capsule, and the experiment at 1.4 GPa used cast octahedra and Fansteel tungsten carbide cubes with 8 mm TEL. At the target pressure, the sample was heated to the target temperature and held for 5 min before quenched by turning off the power. The multi-anvil press is calibrated for pressures above 2 GPa, and therefore a larger pressure error may be present in the experiment at 1.4 GPa where some ceramic parts may not be fully equilibrated under compression.

The experimental products were recovered and examined for texture, composition, and structure. An optical microscope was used to check the position of the electrode tips and thermocouple junctions and locate the Pt sphere in the sample. Raman spectra were collected on a Renishaw Raman microscope for phase identification. Backscattered-electron (BSE) images and energy-dispersive spectra (EDS) were obtained on a JOEL 7800 FLV field emission SEM in the Central Campus Electron Micro-beam Analysis Laboratory (EMAL) at the University of Michigan. The BSE and EDS results were inspected to make sure that products were free of contamination from the four-bore Al_2O_3 tubing, Pt parts or other components in the assembly, which were in direct contact with the sample or might diffuse into the sample.

Diamond-anvil cell experiments

Synchrotron XRD measurements were conducted to investigate the phase stability of $BaCO_3$ at high pressures and high temperatures using a laser-heated diamond-anvil cell (DAC). A symmetric cell with 400 μm culet diamond anvils was used to generate high pressures. A Re gasket was pre-indented to ~35 μm thickness and drilled to form a sample chamber with 200 μm diameter. Fine powders of $BaCO_3$ were mixed with about 5 wt% Pt powder and dried in vacuum oven at 400 K overnight before loading into the DAC. The Pt powder was used as a laser absorber and secondary pressure standard. Two ~10 μm ruby spheres were loaded as the primary pressure standard. The sample was immersed in neon as the pressure transmitting medium and thermal insulator.

Laser heating and angular-dispersive XRD measurements were conducted at the Advanced Photon Source (APS), Beamline 16-ID-B of HPCAT. The sample was heated from both sides by two identical Nd:YLF lasers ($\lambda = 1053$ nm) with 30 μm laser spots. Temperatures were determined by fitting the thermal radiation spectrum to the gray body radiation function (Meng et al. 2015). For a 30 s acquisition time, the temperature measurements yielded readings of 1000–1200 K. The acquisition time was reduced to 15 s at temperatures above 1200 K. The temperature of the heated samples was measured with an accuracy of ±100 K (Errandonea et al. 2003). The X-ray beam was monochromatized to a wavelength of 0.4066 Å and focused to an area of 5.3 × 4.4 μm. Diffraction images were recorded for 15 s with a MAR CCD detector.

Synchrotron XRD patterns of $BaCO_3$ were recorded at temperatures up to 1500 K and at pressures up to 30 GPa. At several pressure points near the phase boundary, the sample was laser-heated at a small power step until a temperature reading could be obtained. A series of XRD patterns of the heated spot were recorded at different temperatures and after quenching to 300 K. The 2D images were integrated into 1D patterns using Dioptas (Prescher and Prakapenka 2015) and refined using the PDIndexer software (Seto et al. 2010).

RESULTS AND DISCUSSION

Melting points of $BaCO_3$ from ionic conductivity and Pt sphere experiments

The melting points of $BaCO_3$ between 3 and 11 GPa were determined in five ionic conductivity experiments (Table 1). At a given pressure, melting was detected on the basis of a steep rise in the ionic current through the sample (Fig. 2 and Supplementary[1] Data). Upon heating, the current through the samples remained at a fairly low value of a few to a few tens of microamps before soaring to several hundred microamps near the melting point. Further heating led to a plateau or smaller rise in current. The current-temperature relation reversed upon cooling, with a steep decrease usually 50 to 100 K lower than the melting point detected

TABLE 1. Experimental conditions and results of ionic conductivity experiments

Exp. ID	P^a (GPa)	T^b (K)
M072815	3.3	2063
	4.1	2028
	5.0	1948
	7.0	1961
	9.0	2240
	10.0[c]	2343
	11.0[c]	2453
M040716	3.3	2087
	4.0	1986
	5.0	1863
	6.0	1933
	7.0	2083
M072717	3.0	2149
	6.0	1843
M080317	5.5	1965
	6.5	2020
	8.0	2197
M080617	7.0	1961
	8.0	2148
	9.0	2253
	10.0[c]	2368

[a] Pressure uncertainty is ±7%.

[b] Temperatures are averages of melting points measurements from at least two heating cycles and uncertainty is ±50 K.

[c] The melting points measured above 10 GPa may have large errors likely due to the melting of Pt.

during heating. The rise and fall of sample current were repeatedly measured over multiple heating and cooling cycles at a given pressure. The rapid rise in ionic current is attributed to the dissociation of crystalline ionic bonding, which is endothermic and reversible. The hysteresis can be explained by supercooling due to the kinetic barrier in nucleation (Galiński et al. 2006), which exists for freezing but not melting, hence we located the melting points based on the steep current rise in the heating cycles.

As reported previously (Li et al. 2017), the pre-melting rise in ionic conductivity measurements introduces uncertainties in locating the melting point (Fig. 2). The current starts to increase at 50 to 100 K below the melting point and ramps up at an increasing rate toward melting, likely due to crystal defects created at high temperatures (Hayes and Hutchings 1989). Different criteria may be adopted to place the onset of melting at the beginning, middle, or end of the steep rise. For consistency, the middle point of the steepest segment of the current-temperature curve, where dI/dT reached the maximum value, was taken as the melting point. The melting points measured in multiple heating cycles at a given pressure typically differ by less than 20 K and the average values are reported (Table 1). Among different experiments, the measured melting temperature at a given pressure agree to within 100 K.

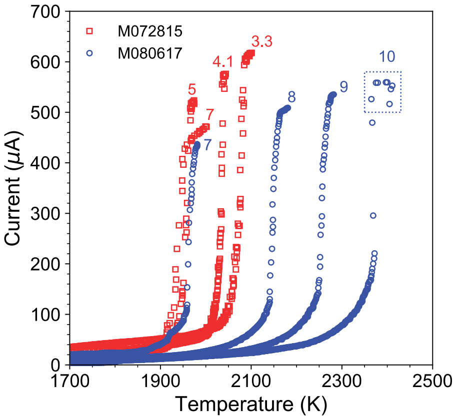

FIGURE 2. Representative current-temperature measurements during heating cycles at high pressures. M072815 (red squares) and M080617 (blue circles). The melting point is located by the maximum of the first derivative of the current (dI/dT). The dashed rectangle (blue) shows fluctuation in the current after melting at 10 GPa, indicating melting of the Pt capsule or electrodes.

In an attempt to measure the melting point of $BaCO_3$ at 1 bar, we heated $BaCO_3$ in a Pt crucible to 1173 K using an electric furnace at the rate of 60 K per minute and then cooled it in the air to room temperature. The sample was then weighed using a Mettler-Toledo balance and examined under a Leica microscope for mass and textural change. Its weight loss clearly indicated decomposition, possibly in combination with melting. The Alfa Aesar value of 1084 K is similar to the witherite-trigonal phase transition at ~1093 K and 1 bar (Antao and Hassan 2007), or it may correspond to the eutectic melting between $BaCO_3$ and BaO at a specific partial pressure of CO_2. A furnace with controlled CO_2 partial pressure is required to determine the melting and decomposition behavior of $BaCO_3$. Here we take the CRC value at 1828 K as the nominal melting point of $BaCO_3$ at 1 bar.

Melting point data from 1 bar to 5 GPa were used to fit a Kechin melting equation (Kechin 2001) (Eq. 1):

$$T_m = T_0 \cdot \left(1 + \frac{P - P_0}{a}\right)^{\frac{1}{b}} \cdot e^{-c(P-P_0)} \tag{1}$$

and melting data above 5.5 GPa were fitted to a second-order polynomial (Eq. 2) from 5.5 to 11 GPa:

$$T_m = p \cdot P^2 + q \cdot P + w \tag{2}$$

where T_m and T_0 are the melting point and the reference temperature in K, and P and P_0 are the pressure and the reference pressure in GPa. Here, the reference condition is the nominal melting point of $BaCO_3$ at 1 bar, $T_0 = 1828$ K and $P_0 = 1$ bar ~0 GPa. Fitted melting curve parameters are $a = 0.0382017$, $b = 11.6106$, $c = 0.0760715$ and $p = -2.684$, $q = 153.6$, w = 1088.

Bounds on the melting point were obtained from four Pt sphere experiments at 1.4, 5.5, and 8 GPa (Table 2). In M120117 and M123117, Pt spheres sank and indicated melting below 2023 K at 5.5 GPa, and below 2223 K at 8 GPa. Experiment M112117 at 5.5 GPa was quenched at 2011 K due to the failure of the heating controller. The Pt sphere also sank in this experiment, suggesting that the melting point at 5.5 GPa is likely lower than 2011 K. In M110917, the Pt sphere remained at the top of the sample, indicating that the melting point at 1.4 GPa is above 2073 K. Although more Pt sphere experiments are required to bracket the melting curve independently, the bounds from the existing Pt sphere experiments are broadly consistent with the results of ionic conductivity measurements within experimental uncertainties and support the adopted criterion for locating the melting point from the current jumps (Fig. 3).

All the recovered samples were confirmed to be $BaCO_3$ and

TABLE 2. Results of Pt sphere experiments

Exp. ID	P (GPa)	T (K)	Result
M110917	1.4	2073	not sink
M112117	5.5	2011	sink
M120117	5.5	2023	sink
M123117	8.0	2223	sink

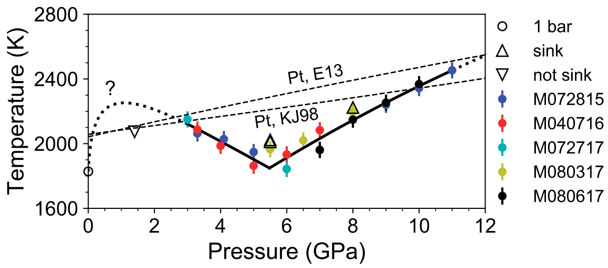

FIGURE 3. Melting curve of $BaCO_3$ at high pressures. The melting curve is established from the ionic conductivity measurements in Table 1 (filled circle with error bar), by fitting the melting points from 1 bar to 5 GPa to a Kechin melting equation (Kechin 2001) and a second-order polynomial from 5.5 to 11 GPa. The melting curve between 1 bar and 3 GPa (dotted line) is back-extrapolated from the Kechin melting curve (Eq. 1) but has not been confirmed experimentally. A melting minimum is located near 5.5 GPa and 1849 K, where the two segments of the fitted melting curve cross. Results of Pt sphere experiments (triangle down = not sink; triangle up = sink) are plotted for cross-validation. The melting curves of Pt (dashed lines = Errandonea 2013 and Kavner and Jeanloz 1998) cross the fitting melting curve of $BaCO_3$ multiple times, near 1 bar, 3 GPa, and 10–12 GPa.

TABLE 3. Lattice parameters of $BaCO_3$ at high pressures and temperatures

P (GPa)	*T* (K)	Space group	*a* (Å)	*b* (Å)	*c* (Å)	*V* (Å^3)
6.3	300	*Pmcn*	4.983(10)	5.425(10)	4.509(8)	121.9(8)
6.3	1026	*Pmmn*	5.080(5)	5.444(5)	4.532(4)	125.3(4)
8.0	300	*Pmcn*	4.931(2)	5.399(2)	4.520(3)	120.3(2)
8.0	1100	*Pmmn*	4.996(1)	5.415(1)	4.529(1)	122.5(1)
9.3	300	*Pmmn*	4.914(8)	5.381(10)	4.523(18)	119.6(11)

Note: Values in parentheses are uncertainties on the last digits.

the atomic ratio of Ba:C:O is approximately 1:1:3. EDS analyses, as well as the texture of the recovered sample, showed no sign of chemical contamination and $BaCO_3$ did not decompose or undergo incongruent melting. In several conductivity experiments, the current reading became unstable when the temperature approached the melting point of the Pt electrode. At 10 GPa in experiment M080617, the current dropped noticeably after the melting temperature was reached (Fig. 2). At this pressure, the melting point of $BaCO_3$ may be still 120 K below that of Pt (Errandonea 2013) or have exceeded the Pt melting temperature (Kavner and Jeanloz 1998). Likewise, the measured melting point of $BaCO_3$ at 3 GPa falls between the two reported Pt melting points at 2180 K (Errandonea 2013) and 2137 K (Kavner and Jeanloz 1998). No sample was recovered from these experiments because the Pt capsules melted. The crossing between the melting curves of $BaCO_3$ and Pt limits the application of this experimental configuration at pressures below 3 GPa and above 10–12 GPa (Fig. 3).

Phase boundary between aragonite and post-aragonite

Synchrotron XRD measurements (Table 3) revealed the phase transformation of $BaCO_3$ from the aragonite structure (*Pmcn*) to the post-aragonite structure (*Pmmn*) at high pressures and/or high temperatures. The post-aragonite phase can be readily recognized by two distinct peaks at 6.36° and 6.70° in the XRD pattern (Fig. 4). Upon compression at 300 K, the phase transformation took place at a pressure between 8 and 9.5 GPa and room temperature. Upon heating to 1026 K at 6.3 GPa, the sample transformed fully to the post-aragonite phase. At 8.1 GPa, the transformation was already complete at 1000 K. The post-aragonite phase remained metastable when the sample was cooled to 1000 K at 6.3 GPa. It was also a metastable phase when the sample was quenched to room temperature at both pressures. Upon decompression to ambient pressure, the post-aragonite phase transformed back to witherite. Our results are consistent with the results from the literature that $BaCO_3$ transforms from aragonite to post-aragonite structure at 7–10 GPa and room temperature (Ono 2007; Ono et al. 2008; Zaoui and Shahrour 2010; Townsend et al. 2013; Wang et al. 2015). Although we could not measure temperatures below 1000 K to determine the transition temperature below 9 GPa, our data suggest that the boundary between the aragonite and post-aragonite phases of $BaCO_3$ likely has a negative slope (Fig. 5). The possibility of a positive boundary (Shatskiy et al. 2015), however, cannot be ruled out because the transition may have been kinetically hindered at low temperatures.

The average thermal expansion coefficient of $BaCO_3$ in the post-aragonite structure is estimated to be 3.9(8) $\times 10^{-5}$ K^{-1} between room temperature and 1026 K at 6.3 GPa and 2.3(2) $\times 10^{-5}$ K^{-1} between room temperature and 1100 K at 8 GPa (Table 3). These preliminary values are comparable to that of $CaCO_3$ (Wu et al. 1995) and $MgCO_3$ (Litasov et al. 2008) but can be better constrained by additional synchrotron XRD experiments.

MELTING CURVE MINIMUM AND SOLID-SOLID PHASE TRANSITION TO POST-ARAGONITE STRUCTURE

Between 3 and 11 GPa, $BaCO_3$ melted over a large range of temperatures up to 2453 K, with a fitted melting curve minimum at 1849 K at 5.5 GPa (Fig. 3). On the low-pressure side of the melting curve minimum, the melting points of $BaCO_3$ decrease continuously from 2149 K at 3 GPa to 1849 K at 5.5 GPa. On the

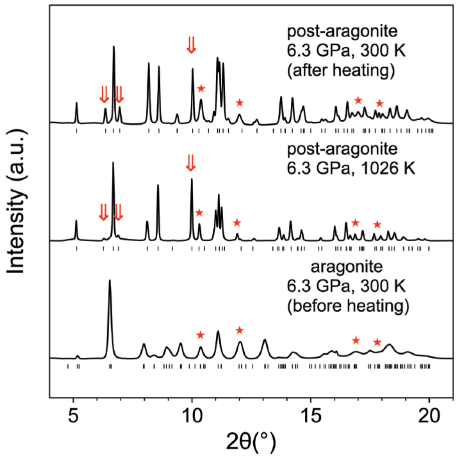

FIGURE 4. Synchrotron XRD experiments show that the aragonite phase $BaCO_3$ transforms into the post-aragonite phase at 6.3 GPa, 1026 K, and the post-aragonite phase was preserved when quenching to ambient temperature. The stars represent the Pt mixed with the sample as a heat absorber. The tick marks show the calculated peak position for aragonite [a = 5.227(4) Å, b = 8.889(12) Å, and c = 5.839(4) Å] and post-aragonite phases [a = 5.800(5) Å, b = 5.444(5) Å, and c = 4.532(4) Å at 1026 K; a = 4.983(10) Å, b = 5.425(10) Å, and c = 4.509(8) Å at 300 K], respectively.

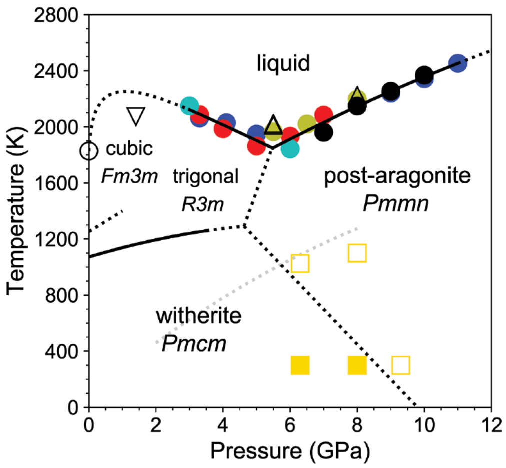

Figure 5. Phase diagram of BaCO$_3$. The boundary between the witherite and post-aragonite BaCO$_3$ (dotted negative slope in black) is drawn according to the synchrotron XRD measurements in Table 3 (open square = post-aragonite BaCO$_3$; filled square = aragonite BaCO$_3$). The dotted positive slope in gray is the same phase boundary proposed in Shatskiy et al. (2015). The phase transition from witherite to trigonal BaCO$_3$ (solid = Rapoport and Pistorius1967) intersects with this proposed witherite-post-aragonite boundary near 5 GPa and 1200 K. Cubic BaCO$_3$ forms at 1 bar and high temperatures, and its stability field at high pressures is not known.

high-pressure side, it increases from 1849 K at 5.5 GPa to 2453 K at 11 GPa. The fitted melting curve changes at a rate of ~–125 K/GPa from 3 GPa, and after reaching the local minimum near 5 GPa, the melting curve increases at a rate of ~110 K/GPa to 11 GPa. The intersection of the fitted melting curves was determined as the local minimum at 1849 K, 5.5 GPa, where the sign of the melting slope flips from negative to positive (Fig. 5).

The local minimum is a prominent feature in the melting curve of BaCO$_3$. According to the Claudius-Clapeyron equation, $dT/dP = \Delta V/\Delta S = T\Delta V/\Delta H$, the slope of the melting curve is governed by the volume of fusion ($\Delta V = V_{\text{liquid}} - V_{\text{solid}}$) and the entropy of fusion ($\Delta S = S_{\text{liquid}} - S_{\text{solid}}$). Melting of a single component is usually an endothermic process with positive ΔH and ΔS, hence the sign of the melting slope is determined by the ΔV term: A positive sign implies that the solid is denser than the liquid, and vice versa. A sign change indicates a density crossover between the liquid and solid. In BaCO$_3$, the flip of the melting slope from negative to positive near 5 GPa indicates a density jump (volume collapse) in the solid phase.

We postulate a trigonal to post-aragonite phase transition is responsible for the density crossover between the solid and liquid near 5.4 GPa. The structures of solid phases along the low-pressure segment of the melting curve are not known. At least three solid polymorphs of BaCO$_3$ occur at pressures up to 6 GPa, including witherite in the aragonite structure, a trigonal calcite structure and a cubic structure (Fig. 5). Upon heating at the ambient pressure, aragonite BaCO$_3$ transforms to the trigonal structure at 1084 K (Antao and Hassan 2007), and then to a cubic structure at 1249 K (Lander 1949; Antao and Hassan 2007; Nie et al. 2017). No further phase change has been observed up to 1573 K at ambient pressure. Previous experiments at pressures up to 3.6 GPa found a slightly positive phase boundary between the aragonite and the trigonal phase (Rapoport and Pistorius 1967). The cubic BaCO$_3$ has not been studied at high pressures and its stability field remains unconstrained. The transition to the cubic structure at 1249 K is thought to be driven by the increased rotational activity of the CO$_3^{2-}$ groups (Lander 1949). Because the rotation is more restricted under compression, the cubic structure may become thermodynamically less favored at elevated pressures. For these reasons, we postulate that the trigonal phase is likely the high-temperature BaCO$_3$ polymorph on the melting curve just below 5.5 GPa. On the high-pressure side of the melting curve minimum, the BaCO$_3$ polymorph below the melting curve is not fully resolved but the post-aragonite structure has been shown to be stable at high temperature over a broad range of pressures (e.g., Townsend et al. 2013). Assuming the post-aragonite BaCO$_3$ is the only stable phase on the high-pressure side of the melting curve minimum, the aragonite-trigonal boundary intersects with the negative phase boundary between the aragonite and post-aragonite at a triple point near 5 GPa and 1200 K, suggesting the presence of a boundary between trigonal and post-aragonite, which is defined by the triple point and the melting curve minimum. This boundary implies that the melting curve minimum may correspond to a triple point where liquid, trigonal, and post-aragonite phase of BaCO$_3$ coexist (Fig. 5).

The coordination number of Ba is 6 in the trigonal structure and 12 in the post-aragonite structure (Ono et al. 2008). The difference in the coordination of Ba would make the post-aragonite phase denser than the trigonal phase and could explain the density jump at the melting minimum near 5 GPa (Fig. 6). Current knowledge of solid-solid phase transformations of BaCO$_3$ is insufficient to map out the phase diagram, and therefore the melting curve minimum may be associated with other solid-solid phase transitions involving different coordination number of Ba. In addition, several metastable phases of BaCO$_3$ have been observed experimentally. A $P2_122$ rhombohedral phase was also recovered from the experiment at 15 GPa and 1273 K (Lin and Liu 1997), while a phase transition to the trigonal phase ($P31c$) was observed at 7.2 GPa and room temperature (Holl et al. 2000; Chaney et al. 2015).

Melting curve maximum and possible change in liquid structure

The presence of a melting curve maximum in BaCO$_3$ is suggested by our experimental data and existing constraints on the melting point at 1 bar. According to the 98th edition of the *CRC Handbooks of Chemistry and Physics*, the melting point at 1 bar is 1828 K, whereas Alfa Aesar Materials Safety Data Sheet (ThermoFisher Scientific 2010) listed 1084 K as the melting point, which is most likely the boundary between the aragonite and trigonal phase. Some studies found that BaCO$_3$ started decomposing at 1200 K to produce BaO and CO$_2$ vapors (L'vov and Novichikhin 1997) and decomposition proceeds in a melt after 1300 K (Galwey and Brown 1999). The prevailing CO$_2$ pressure is known to influence its melting behavior (Judd and Pope 1972). Despite the uncertainties, the melting point of BaCO$_3$ at 1 bar is likely equal to or less than 1828 K. Our Pt sphere experiment indicates that the melting point at 1.4 GPa is above 2073 K, and therefore the melting curve has a positive slope at elevated pressures near 1 bar. Between 3 and 5.4 GPa, a negative melting slope determined by our conductivity measurements implies that a local maximum of

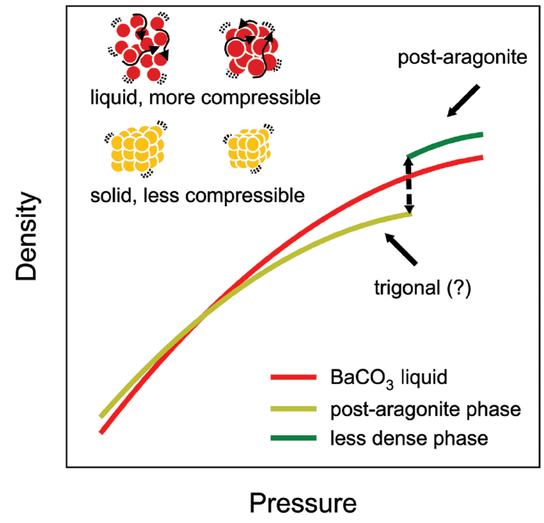

FIGURE 6. Schematic density profiles of liquid $BaCO_3$, post-aragonite $BaCO_3$, and a less dense $BaCO_3$ phase, likely the trigonal phase, at a constant temperature. On the high-pressure side, the phase transformation from aragonite $BaCO_3$ (witherite) to post-aragonite $BaCO_3$ causes an abrupt density change in the solid. The post-aragonite $BaCO_3$ becomes denser than liquid $BaCO_3$ above 5.5 GPa, whereas the compressed liquid $BaCO_3$ is denser than the solid from 3 to 5.5 GPa (solid line), which explains the melting curve minimum near 5 GPa. On the low-pressure side, the compressed liquid is less dense than the solid (dashed line), which explains the inferred melting curve maximum.

the melting curve occurs between 1 bar and 3 GPa.

The local maximum implies another density crossover between solid and liquid, which can be attributed to continuous changes in the liquid structure. Without long-range orders, the liquid structure is more flexible and may allow the coexistence of multiple coordination numbers (Ghiorso 2004; Stixrude and Karki 2005) and polyhedra configurations (Liu et al. 2007). As pressure increases, the average coordination number of $BaCO_3$ in the liquid may increase continuously whereas the solid phase has a fixed coordination number until a pressure-induced, discontinuous phase transition takes place. As a result, the liquid would be more compressible than the solid and have a density equals to that of the solid at the melting point maximum. If the density crossover arises from the more compressible liquid, the volume difference between the solid and liquid would increase continuously away from the local maximum, and therefore the slopes of the melting curves are expected to flatten gradually near the turning point.

However, the occurrence of liquid structure change in $BaCO_3$ need to be further confirmed by future theoretical and/or experimental investigation, and this particular hypothesis remains highly speculative.

Systematic comparison of alkaline earth carbonates

The shape of the melting curve of $BaCO_3$ resembles that of $CaCO_3$, but the melting curve minimum is more pronounced and occurs at lower pressure (Fig. 7a). In $CaCO_3$, a local maximum was observed near 8 GPa, and a local minimum occurs near 13 GPa. The negative melting slope in $CaCO_3$ between 8 and 13 GPa is indicated by melting points collected at multiple pressures in individual conductivity experiment, but the sign of the slope cannot be resolved when data from different experiments are combined (Li et al. 2017). The negative slope of $BaCO_3$ from 3 to 5 GPa and the positive slope at pressures above 6 GPa are both steep and have been clearly observed experimentally. In contrast, limited data suggest that the melting point of $MgCO_3$ increases monotonically up to 15 GPa (Irving and Wyllie 1973; Katsura and Ito 1990; Müller et al. 2017) and tends to flatten at higher pressures up to 80 GPa (Solopova et al. 2015).

The occurrence or absence of the solid-solid phase transitions below the melting curve in $MgCO_3$, $CaCO_3$, and $BaCO_3$ follow the expected inverse relation between the pressure of structure transformation (Prewitt and Downs 1998; Redfern 2000) and ionic radius ($Ba^{2+} > Ca^{2+} > Mg^{2+}$). At the ambient temperature, $BaCO_3$ (witherite) undergoes the aragonite to post-aragonite phase

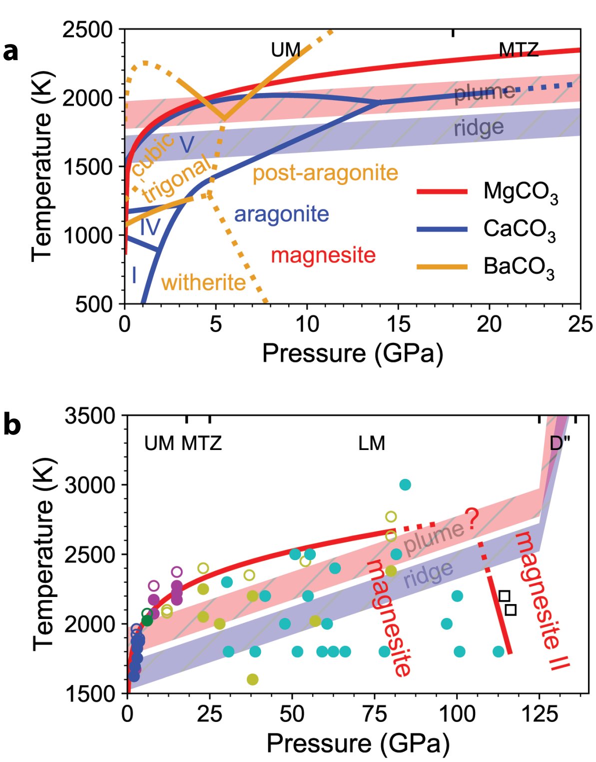

FIGURE 7. Systematic comparison of melting behavior of alkaline earth carbonates. (**a**) The melting curves of $CaCO_3$ (Li et al. 2017) and $BaCO_3$ (this study) do not increase monotonically but have local minima, which significantly decrease melting point at high pressures and affect the order of melting of alkaline earth carbonates. Phase relations of $CaCO_3$ are based on Li et al. (2017) and Bayarjargal et al. (2018). (**b**) No local minimum has been observed in $MgCO_3$, however, a similar melting curve minimum may exist in $MgCO_3$ resulting from the predicted phase transformation to the magnesite II phase (black open square) at megabar pressures (Isshiki et al. 2003) and possibly generate carbonate melt near core-mantle boundary or even in the lower mantle. The melting curve of $MgCO_3$ (red) is a preliminary fit of the existing data to the Kechin melting equation ($a = 0.0005086$, $b = 11.06$, $c = -0.0003971$, $T_0 = 875$ K, and P_0 = 1 bar). Experimental data on $MgCO_3$ were compiled from the literature: blue for Irving and Wyllie (1973), magenta for Katsura and Ito (1990), cyan for Isshiki et al. (2003), yellow for Solopova et al. (2015), and green for Müller et al. (2017) (open circle = liquid $MgCO_3$; filled circle = solid $MgCO_3$). Mantle adiabats were estimated based on Herzberg et al. (2007) and Putirka et al. (2007) with a constant slope of dT/dP = 8 K/GPa.

transition at 9 GPa and the same transition occurs at much higher pressure of near 40 GPa for $CaCO_3$, whereas the trigonal phase of $MgCO_3$ (magnesite) remains stable up to 80 GPa (Fiquet et al. 2002; Isshiki et al. 2004). The melting minimum in $CaCO_3$ at 13 GPa is attributed to a transition from sixfold-coordinated calcite V to ninefold-coordinated aragonite phase (Fig. 7a), whereas that in $BaCO_3$ near 5 GPa likely results from a trigonal to post-aragonite transition. The lack of a melting curve minimum in $MgCO_3$ up to 80 GPa is consistent with the stability of the trigonal phase (Fiquet et al. 2002; Isshiki et al. 2004).

Although the systematics of the solid structures of alkaline earth carbonates is consistent at moderate pressures, the formation of tetrahedrally coordinated carbon at high pressures indicates a deviation from the systematic behavior at megabar pressures (Boulard et al. 2015). Synchrotron XRD measurements (Townsend et al. 2013) and ab initio calculations (Arapan et al. 2007) showed that that the post-aragonite structure of $BaCO_3$ remained the thermodynamically favored phase up to at least 300 GPa. The phase transformation to the pyroxene-type ($C222_1$) $BaCO_3$ was predicted to occur at 76 GPa (Zaoui and Shahrour 2010), whereas it was not observed experimentally at the pressure of at least 150 GPa (Townsend et al. 2013). This observation seems to violate the expected systematic trend that isostructural compounds exhibit the same type of pressure-induced phase transformation and that the transition pressure is lower for larger cation (Prewitt and Downs 1998).

IMPLICATIONS

In this study, we found that the melting curve of $BaCO_3$ involves a local minimum near 5 GPa and may contain a local maximum between ambient pressure and 3 GPa. Density crossovers at the turning points are attributed to structural changes of the relevant phases along the melting curve, including solid-solid transition with an abrupt change in the coordination number of divalent cation and/or gradual increase in the average coordination number in the liquid. The experimentally observed melting curve minima in both $CaCO_3$ and $BaCO_3$ imply that the solid-state transitions in other alkaline earth carbonates may be used to predict the occurrence of turning points in their melting curves. Given the systematic similarity of phase transformation in compressed carbonates, a minimum may occur in $MgCO_3$ at the megabar pressure range where its melting curve intersects the phase transition from magnesite to magnesite II (Fig. 7b).

Accordingly, we may expect a melting curve maximum in $MgCO_3$ resulting from the predicted transition from trigonal phase to a denser polymorph with higher coordination number at megabar pressures (Shatskiy et al. 2015; Isshiki et al. 2004) if the comparative crystal chemistry rules still hold (Hazen et al. 2000). Previous studies suggest that the decomposition boundary of magnesite contains a minimum near 115 GPa (Isshiki et al. 2004). It is conceivable that a similar minimum exists in the melting curve of $MgCO_3$.

The occurrence of melting curve minima at different pressures implies that the order of alkaline-earth carbonate melting points changes with pressure. $BaCO_3$ is less refractory than $MgCO_3$ and $CaCO_3$ near 5.5 GPa but more refractory at other pressures (Fig. 7). The melting curve minima of various carbonates set the upper bound on the solidi of melting in multi-component carbonated rocks. It also dictates the composition of the incipient melt. Therefore, the solidus of a carbonated rock may have variable slopes, and its composition may change considerably with pressure.

Discontinuous change in the slope of the melting curve is a general feature of silicate and alkaline earth carbonates, and therefore melting curves cannot be extrapolated beyond the measurement range without considering adjacent solid-solid transitions. The empirical Simon equation has been widely used to fit high-pressure melting curves (e.g., Li and Li 2015). This melting equation has the advantage of not requiring any knowledge of the solid's equation of state and works well for interpolation. For a negative segment of the melting curve, however, the empirical Simon equation must be modified to describe the negative pressure dependence of melting temperature (Kechin 2001). Lindemann's law provides a semi-empirical scaling relation to fit discrete measurements of melting temperatures for interpolation, and in the absence of data it is often used with an equation of state to predict melting temperatures at high pressures (e.g., Li and Li 2015). Because Lindemann's law does not consider the liquid behavior, it is inadequate to represent flat or negative melting slope associated with structural changes in the liquid.

Constraints on the melting curves shed light on the adjacent high-temperature solid polymorphs. For $BaCO_3$ the melting curve minimum is interpreted as a triple point among liquid, trigonal, and post-aragonite phases. The inferred boundary between the trigonal and post-aragonite phases need to be mapped out by measurements. Furthermore, the boundary between aragonite and post-aragonite may be narrowed down through XRD or Raman measurements using externally heated diamond-anvil cells, where temperatures between room temperature and 1500 K can be more precisely controlled and reliably measured to allow evaluation of kinetic effects and reversal of phase transitions.

Knowledge of the melting curves can also be used to establish the equation-of-state of carbonate melts and help construct thermodynamic models to predict the behavior of carbonate-bearing rocks inside the Earth (e.g., Liu and Lange 2003). This approach is less straightforward in the multi-component melt (Walker et al. 1988) but has been shown to work for carbonate melt (e.g., Liu et al. 2007). For $BaCO_3$, additional experiments are required to determine the melting curve between 1 bar and 3 GPa in the piston-cylinder press, to test the presence of a local maximum and resolve its exact location. In particular, the experimental configuration of the ionic conductivity method needs to be modified for measurements at a few gigapascals using a piston-cylinder press. More refractory materials such as Ir are needed to replace the Pt capsule and electrodes for ionic conductivity measurements on $BaCO_3$ at pressures below 3 GPa and beyond 11 GPa.

FUNDING AND ACKNOWLEDGMENTS

This work was supported by Alfred P. Sloan Foundation grant G-2016-7157 and grant G-2017-9954, and by National Science Foundation grant EAR 1763189, and grant AST 1344133. In addition, we thank Cassandra Seltzer for her assistance with the platinum sphere experiments; David Walker and Matthew Brennan for discussions and comments on the manuscript.

REFERENCES CITED

Antao, S.M., and Hassan, I. (2007) $BaCO_3$: high-temperature crystal structures and the *Pmcn* → *R*3*m* phase transition at 811 °C. Physics and Chemistry of Minerals, 34(8), 573–580.

Arapan, S., De Almeida, J.S., and Ahuja, R. (2007) Formation of sp^3 hybridized bonds and stability of $CaCO_3$ at very high pressure. Physical Review Letters, 98(26), 268501.

Arvanitidis, I., Siche, D., and Seetharaman, S. (1996) A study of the thermal decomposition of $BaCO_3$. Metallurgical and Materials Transactions B, 27(3), 409–416.

Bayarjargal, L., Fruhner, C.J., Schrodt, N., and Winkler, B. (2018) $CaCO_3$ phase diagram studied with Raman spectroscopy at pressures up to 50 GPa and high temperatures and DFT modeling. Physics of the Earth and Planetary Interiors, 281, 31–45.

Boulard, E., Pan, D., Galli, G., Liu, Z., and Mao, W.L. (2015) Tetrahedrally coordinated carbonates in Earth's lower mantle. Nature Communications, 6, 6311.

Chaney, J., Santillán, J.D., Knittle, E., and Williams, Q. (2015) A high-pressure infrared and Raman spectroscopic study of $BaCO_3$: the aragonite, trigonal and *Pmmn* structures. Physics and Chemistry of Minerals, 42(1), 83–93.

Dasgupta, R. (2013) Ingassing, storage, and outgassing of terrestrial carbon through geologic time. Reviews in Mineralogy and Geochemistry, 75, 183–229.

Errandonea, D. (2013) High-pressure melting curves of the transition metals Cu, Ni, Pd, and Pt. Physical Review B, 87(5), 054108.

Errandonea, D., Somayazulu, M., Häusermann, D., and Mao, H.K. (2003) Melting of tantalum at high pressure determined by angle dispersive X-ray diffraction in a double-sided laser-heated diamond-anvil cell. Journal of Physics: Condensed Matter, 15(45), 7635.

Fiquet, G., Guyot, F., Kunz, M., Matas, J., Andrault, D., and Hanfland, M. (2002) Structural refinements of magnesite at very high pressure. American Mineralogist, 87, 1261–1265.

Galiński, M., Lewandowski, A., and Stępniak, I. (2006) Ionic liquids as electrolytes. Electrochimica Acta, 51, 5567–5580.

Galwey, A.K., and Brown, M.E. (1999) Thermal Decomposition of Ionic Solids: Chemical properties and reactivities of ionic crystalline phases, vol. 86. Elsevier.

Ghiorso, M.S. (2004) An equation of state for silicate melts. I. Formulation of a general model. American Journal of Science, 304(8-9), 637–678.

Hayes, W., and Hutchings, M.T. (1989) Ionic Disorder in Crystals at High Temperatures with Emphasis on Fulorites. In Ionic Solids at High Temperatures, pp. 247–362.

Hazen, R.M., Downs, R.T., and Prewitt, C.T. (2000) Principles of comparative crystal chemistry. Reviews in Mineralogy and Geochemistry, 41, 1–33.

Herzberg, C., Asimow, P.D., Arndt, N., Niu, Y., Lesher, C.M., Fitton, J.G., Cheadle, M.J., and Saunders, A.D. (2007) Temperatures in ambient mantle and plumes: Constraints from basalts, picrites, and komatiites. Geochemistry, Geophysics, Geosystems, 8(2).

Holl, C.M., Smyth, J.R., Laustsen, H.M.S., Jacobsen, S.D., and Downs, R.T. (2000) Compression of witherite to 8 GPa and the crystal structure of $BaCO_3$ II. Physics and Chemistry of Minerals, 27(7), 467–473.

Hurt, S.M., and Wolf, A.S. (2018) Thermodynamic properties of $CaCO_3$–$SrCO_3$–$BaCO_3$ liquids: a molecular dynamics study using new empirical atomic potentials for alkaline earth carbonates. Physics and Chemistry of Minerals, 1–16.

Irving, A.J., and Wyllie, P.J. (1973) Melting relationships in CaO-CO_2 and MgO-CO_2 to 36 kilobars with comments on CO_2 in the mantle. Earth and Planetary Science Letters, 20(2), 220–225.

Isshiki, M., Irifune, T., Hirose, K., Ono, S., Ohishi, Y., Watanuki, T., Nishibori, E., Takata, M., and Sakata, M. (2004) Stability of magnesite and its high-pressure form in the lowermost mantle. Nature, 427, 60–63.

Judd, M.D., and Pope, M.I. (1972) Energy of activation for the decomposition of the alkaline-earth carbonates from thermogravimetric data. Journal of Thermal Analysis, 4(1), 31–38.

Katsura, T., and Ito, E. (1990) Melting and subsolidus phase relations in the $MgSiO_3$-$MgCO_3$ system at high pressures: implications to evolution of the Earth's atmosphere. Earth and Planetary Science Letters, 99(1-2), 110–117.

Kavner, A., and Jeanloz, R. (1998) High-pressure melting curve of platinum. Journal of Applied Physics, 83(12), 7553–7559.

Kechin, V.V. (2001) Melting curve equations at high pressure. Physical Review B, 65(5), 052102.

Lander, J.J. (1949) Polymorphism and anion rotational disorder in the alkaline earth carbonates. The Journal of Chemical Physics, 17(10), 892–901.

Leinenweber, K.D., Tyburczy, J.A., Sharp, T.G., Soignard, E., Diedrich, T., Petuskey, W.B., Wang, Y., and Mosenfelder, J.L. (2012) Cell assemblies for reproducible multi-anvil experiments (the COMPRES assemblies). American Mineralogist, 97, 353–368.

Li, Z., and Li, J. (2015) Melting curve of NaCl to 20 GPa from electrical measurements of capacitive current. American Mineralogist, 100, 1892–1898.

Li, J., Hadidiacos, C., Mao, H.K., Fei, Y., and Hemley, R.J. (2003) Behavior of thermocouples under high pressure in a multi-anvil apparatus. High Pressure Research, 23(4), 389–401.

Li, Z., Li, J., Lange, R., Liu, J., and Militzer, B. (2017) Determination of calcium carbonate and sodium carbonate melting curves up to Earth's transition zone pressures with implications for the deep carbon cycle. Earth and Planetary Science Letters, 457, 395–402.

Lin, C.C., and Liu, L.G. (1997) High-pressure Raman spectroscopic study of post-aragonite phase transition in witherite ($BaCO_3$). European Journal of Mineralogy, 9(4), 785–792.

Litasov, K.D., Fei, Y., Ohtani, E., Kuribayashi, T., and Funakoshi, K. (2008) Thermal equation of state of magnesite to 32 GPa and 2073 K. Physics of the Earth and Planetary Interiors, 168(3), 191–203.

Liu, Q., and Lange, R.A. (2003) New density measurements on carbonate liquids and the partial molar volume of the $CaCO_3$ component. Contributions to Mineralogy and Petrology, 146(3), 370–381.

Liu, Q., Tenner, T.J., and Lange, R.A. (2007) Do carbonate liquids become denser than silicate liquids at pressure? Constraints from the fusion curve of K_2CO_3 to 3.2 GPa. Contributions to Mineralogy and Petrology, 153(1), 55–66.

L'vov, B.V., and Novichikhin, A.V. (1997) Quantitative interpretation of the evaporation coefficients for the decomposition or sublimation of some substances in vacuo. Thermochimica Acta, 290(2), 239–251.

Meng, Y., Hrubiak, R., Rod, E., Boehler, R., and Shen, G. (2015) New developments in laser-heated diamond anvil cell with *in situ* synchrotron X-ray diffraction at High Pressure Collaborative Access Team. Review of Scientific Instruments, 86(7), 072201.

Müller, J., Koch-Müller, M., Rhede, D., Wilke, F.D., and Wirth, R. (2017) Melting relations in the system $CaCO_3$-$MgCO_3$ at 6 GPa. American Mineralogist: Journal of Earth and Planetary Materials, 102(12), 2440–2449.

Nie, S., Liu, Y., Liu, Q., Wang, M., and Wang, H. (2017) Phase transitions and thermal expansion of $BaCO_3$ and $SrCO_3$ up to 1413 K. European Journal of Mineralogy, 29(3), 433–443.

Ono, S. (2007) New high-pressure phases in $BaCO_3$. Physics and Chemistry of Minerals, 34(4), 215–221.

Ono, S., Brodholt, J.P., and Price, G.D. (2008) Phase transitions of $BaCO_3$ at high pressures. Mineralogical Magazine, 72(2), 659–665.

Prescher, C., and Prakapenka, V.B. (2015) DIOPTAS: a program for reduction of two-dimensional X-ray diffraction data and data exploration. High Pressure Research, 35(3), 223–230.

Prewitt, C.T., and Downs, R.T. (1998) High-pressure crystal chemistry. Reviews in Mineralogy, 37, 284–318.

Putirka, K.D., Perfit, M., Ryerson, F.J., and Jackson, M.G. (2007) Ambient and excess mantle temperatures, olivine thermometry, and active vs. passive upwelling. Chemical Geology, 241(3-4), 177–206.

Rapoport, E., and Pistorius, C.W. (1967) Orthorhombic-disordered rhombohedral transition in $SrCO_3$ and $BaCO_3$ to 40 kilobars. Journal of Geophysical Research, 72(24), 6353–6357.

Redfern, S.A. (2000) Structural variations in carbonates. Reviews in Mineralogy and Geochemistry, 41, 289–308.

Rumble, J.R. (Ed.). (2018) CRC Handbook of Chemistry and Physics, 98th ed. (internet ver. 2018). CRC Press, Taylor and Francis.

Seto, Y., Nishio-Hamane, D., Nagai, T., and Sata, N. (2010). Development of a software suite on X-ray diffraction experiments. Review of High Pressure Science and Technology, 20(3).

Shatskiy, A.F., Litasov, K.D., and Palyanov, Y.N. (2015) Phase relations in carbonate systems at pressures and temperatures of lithospheric mantle: review of experimental data. Russian Geology and Geophysics, 56(1-2), 113–142.

Solopova, N.A., Dubrovinsky, L., Spivak, A.V., Litvin, Y.A., and Dubrovinskaia, N. (2015) Melting and decomposition of $MgCO_3$ at pressures up to 84 GPa. Physics and Chemistry of Minerals, 42(1), 73–81.

Stern, K.H., and Weise, E.L. (Eds.). (1969) High temperature properties and decomposition of inorganic salts, Part II: Carbonates. National Standard Reference Data System (NSRDS-NBS 30). National Bureau of Standards, 12–13.

Stixrude, L., and Karki, B. (2005) Structure and freezing of $MgSiO_3$ liquid in Earth's lower mantle. Science, 310, 297–299.

ThermoFisher Scientific (2010) Barium carbonate; MSDS No. 10645. Alfa Aesar Thermo Fisher Scientific Chemicals: Ward Hill, Massachusetts (accessed June 2, 2018). https://www.alfa.com/en/content/msds/USA/10645.pdf

Townsend, J.P., Chang, Y.Y., Lou, X., Merino, M., Kirklin, S.J., Doak, J.W., Issa, A., Wolverton, C., Tkachev, S.N., Dera, P., and Jacobsen, S.D. (2013) Stability and equation of state of post-aragonite $BaCO_3$. Physics and Chemistry of Minerals, 40(5), 447–453.

Walker, D., Agee, C.B., and Zhang, Y. (1988) Fusion curve slope and crystal/liquid buoyancy. Journal of Geophysical Research: Solid Earth, 93(B1), 313–323.

Wang, M., Liu, Q., Nie, S., Li, B., Wu, Y., Gao, J., Wei, X., and Wu, X. (2015) High-pressure phase transitions and compressibilities of aragonite-structure carbonates: $SrCO_3$ and $BaCO_3$. Physics and Chemistry of Minerals, 42(6), 517–527.

Wu, T.C., Shen, A.H., Weathers, M.S., Bassett, W.A., and Chou, I.M. (1995) Anisotropic thermal expansion of calcite at high pressures: An in situ X-ray diffraction study in a hydrothermal diamond-anvil cell. American Mineralogist, 80, 941–946.

Zaoui, A., and Shahrour, I. (2010) Molecular dynamics study of high-pressure polymorphs of $BaCO_3$. Philosophical Magazine Letters, 90(9), 689–697.

Manuscript received November 12, 2018
Manuscript accepted February 11, 2019
Manuscript handled by Simon Redfern

Endnote:

[1] Deposit item AM-19-56891, Supplemental Material. Deposit items are free to all readers and found on the MSA website, via the specific issue's Table of Contents (go to http://www.minsocam.org/MSA/AmMin/TOC/2019/May2019_data/May2019_data.html).